DESY 95-251

DESY 95-251
December 1995

hep-ex/9601004 15 Jan 1996

Elastic Photoproduction of ρ^0 Mesons at HERA

H1 Collaboration

Abstract

The cross section for the elastic photoproduction of ρ^0 mesons ($\gamma p \to \rho^0 p$) has been measured with the H1 detector at HERA for two average photon-proton centre-of-mass energies of 55 and 187 GeV. The lower energy point was measured by observing directly the ρ^0 decay giving a cross section of $9.1 \pm 0.9\,(\text{stat.}) \pm 2.5\,(\text{syst.})\ \mu$b. The logarithmic slope parameter of the differential cross section, $\mathrm{d}\sigma/\mathrm{d}t$, is found to be $10.9 \pm 2.4\,(\text{stat.}) \pm 1.1\,(\text{syst.})\ \text{GeV}^{-2}$. The ρ^0 decay polar angular distribution is found to be consistent with s-channel helicity conservation. The higher energy cross section was determined from analysis of the lower part of the hadronic invariant mass spectrum of diffractive photoproduction and found to be $13.6 \pm 0.8\,(\text{stat.}) \pm 2.4\,(\text{syst.})\ \mu$b.

S. Aid[14], V. Andreev[26], B. Andrieu[29], R.-D. Appuhn[12], M. Arpagaus[37], A. Babaev[25], J. Bähr[36], J. Bán[18], Y. Ban[28], P. Baranov[26], E. Barrelet[30], R. Barschke[12], W. Bartel[12], M. Barth[5], U. Bassler[30], H.P. Beck[38], H.-J. Behrend[12], A. Belousov[26], Ch. Berger[1], G. Bernardi[30], R. Bernet[37], G. Bertrand-Coremans[5], M. Besançon[10], R. Beyer[12], P. Biddulph[23], P. Bispham[23], J.C. Bizot[28], V. Blobel[14], K. Borras[9], F. Botterweck[5], V. Boudry[29], A. Braemer[15], W. Braunschweig[1], V. Brisson[28], D. Bruncko[18], C. Brune[16], R. Buchholz[12], L. Büngener[14], J. Bürger[12], F.W. Büsser[14], A. Buniatian[12,39], S. Burke[19], M.J. Burton[23], G. Buschhorn[27], A.J. Campbell[12], T. Carli[27], F. Charles[12], M. Charlet[12], D. Clarke[6], A.B. Clegg[19], B. Clerbaux[5], S. Cocks[20], J.G. Contreras[9], C. Cormack[20], J.A. Coughlan[6], A. Courau[28], M.-C. Cousinou[24], Ch. Coutures[10], G. Cozzika[10], L. Criegee[12], D.G. Cussans[6], J. Cvach[31], S. Dagoret[30], J.B. Dainton[20], W.D. Dau[17], K. Daum[35], M. David[10], C.L. Davis[19], B. Delcourt[28], A. De Roeck[12], E.A. De Wolf[5], M. Dirkmann[9], P. Dixon[19], P. Di Nezza[33], W. Dlugosz[8], C. Dollfus[38], J.D. Dowell[4], H.B. Dreis[2], A. Droutskoi[25], D. Düllmann[14], O. Dünger[14], H. Duhm[13], J. Ebert[35], T.R. Ebert[20], G. Eckerlin[12], V. Efremenko[25], S. Egli[38], R. Eichler[37], F. Eisele[15], E. Eisenhandler[21], R.J. Ellison[23], E. Elsen[12], M. Erdmann[15], W. Erdmann[37], E. Evrard[5], A.B. Fahr[14], L. Favart[5], A. Fedotov[25], D. Feeken[14], R. Felst[12], J. Feltesse[10], J. Ferencei[18], F. Ferrarotto[33], K. Flamm[12], M. Fleischer[9], M. Flieser[27], G. Flügge[2], A. Fomenko[26], B. Fominykh[25], M. Forbush[8], J. Formánek[32], J.M. Foster[23], G. Franke[12], E. Fretwurst[13], E. Gabathuler[20], K. Gabathuler[34], F. Gaede[27], J. Garvey[4], J. Gayler[12], M. Gebauer[9], A. Gellrich[12], H. Genzel[1], R. Gerhards[12], A. Glazov[36], U. Goerlach[12], L. Goerlich[7], N. Gogitidze[26], M. Goldberg[30], D. Goldner[9], K. Golec-Biernat[7], B. Gonzalez-Pineiro[30], I. Gorelov[25], C. Grab[37], H. Grässler[2], R. Grässler[2], T. Greenshaw[20], R. Griffiths[21], G. Grindhammer[27], A. Gruber[27], C. Gruber[17], J. Haack[36], D. Haidt[12], L. Hajduk[7], M. Hampel[1], M. Hapke[12], W.J. Haynes[6], G. Heinzelmann[14], R.C.W. Henderson[19], H. Henschel[36], I. Herynek[31], M.F. Hess[27], W. Hildesheim[12], K.H. Hiller[36], C.D. Hilton[23], J. Hladký[31], K.C. Hoeger[23], M. Höppner[9], D. Hoffmann[12], T. Holtom[20], R. Horisberger[34], V.L. Hudgson[4], M. Hütte[9], H. Hufnagel[15], M. Ibbotson[23], H. Itterbeck[1], M.-A. Jabiol[10], A. Jacholkowska[28], C. Jacobsson[22], M. Jaffre[28], J. Janoth[16], T. Jansen[12], L. Jönsson[22], K. Johannsen[14], D.P. Johnson[5], L. Johnson[19], H. Jung[10], P.I.P. Kalmus[21], M. Kander[12], D. Kant[21], R. Kaschowitz[2], U. Kathage[17], J. Katzy[15], H.H. Kaufmann[36], S. Kazarian[12], I.R. Kenyon[4], S. Kermiche[24], C. Keuker[1], C. Kiesling[27], M. Klein[36], C. Kleinwort[12], G. Knies[12], W. Ko[8], T. Köhler[1], J.H. Köhne[27], H. Kolanoski[3], F. Kole[8], S.D. Kolya[23], V. Korbel[12], M. Korn[9], P. Kostka[36], S.K. Kotelnikov[26], T. Krämerkämper[9], M.W. Krasny[7,30], H. Krehbiel[12], D. Krücker[2], U. Krüger[12], U. Krüner-Marquis[12], H. Küster[22], M. Kuhlen[27], T. Kurča[36], J. Kurzhöfer[9], D. Lacour[30], B. Laforge[10], F. Lamarche[29], R. Lander[8], M.P.J. Landon[21], W. Lange[36], U. Langenegger[37], P. Lanius[27], J.-F. Laporte[10], A. Lebedev[26], F. Lehner[12], C. Leverenz[12], S. Levonian[26], Ch. Ley[2], G. Lindström[13], M. Lindstroem[22], J. Link[8], F. Linsel[12], J. Lipinski[14], B. List[12], G. Lobo[28], P. Loch[28], H. Lohmander[22], J.W. Lomas[23], G.C. Lopez[13], V. Lubimov[25], D. Lüke[9,12], N. Magnussen[35], E. Malinovski[26], S. Mani[8], R. Maraček[18], P. Marage[5], J. Marks[24], R. Marshall[23], J. Martens[35], G. Martin[14], R. Martin[20], H.-U. Martyn[1], J. Martyniak[7], S. Masson[2], T. Mavroidis[21], S.J. Maxfield[20], S.J. McMahon[20], A. Mehta[6], K. Meier[16], T. Merz[36], A. Meyer[12], A. Meyer[14], H. Meyer[35], J. Meyer[12], P.-O. Meyer[2], A. Migliori[29], S. Mikocki[7], D. Milstead[20], J. Moeck[27], F. Moreau[29], J.V. Morris[6],

E. Mroczko[7], D. Müller[38], G. Müller[12], K. Müller[12], P. Murín[18], V. Nagovizin[25], R. Nahnhauer[36], B. Naroska[14], Th. Naumann[36], P.R. Newman[4], D. Newton[19], D. Neyret[30], H.K. Nguyen[30], T.C. Nicholls[4], F. Niebergall[14], C. Niebuhr[12], Ch. Niedzballa[1], H. Niggli[37], R. Nisius[1], G. Nowak[7], G.W. Noyes[6], M. Nyberg-Werther[22], M. Oakden[20], H. Oberlack[27], U. Obrock[9], J.E. Olsson[12], D. Ozerov[25], P. Palmen[2], E. Panaro[12], A. Panitch[5], C. Pascaud[28], G.D. Patel[20], H. Pawletta[2], E. Peppel[36], E. Perez[10], J.P. Phillips[20], A. Pieuchot[24], D. Pitzl[37], G. Pope[8], S. Prell[12], R. Prosi[12], K. Rabbertz[1], G. Rädel[12], F. Raupach[1], P. Reimer[31], S. Reinshagen[12], H. Rick[9], V. Riech[13], J. Riedlberger[37], F. Riepenhausen[2], S. Riess[14], M. Rietz[2], E. Rizvi[21], S.M. Robertson[4], P. Robmann[38], H.E. Roloff[36], R. Roosen[5], K. Rosenbauer[1], A. Rostovtsev[25], F. Rouse[8], C. Royon[10], K. Rüter[27], S. Rusakov[26], K. Rybicki[7], N. Sahlmann[2], D.P.C. Sankey[6], P. Schacht[27], S. Schiek[14], S. Schleif[16], P. Schleper[15], W. von Schlippe[21], D. Schmidt[35], G. Schmidt[14], A. Schöning[12], V. Schröder[12], E. Schuhmann[27], B. Schwab[15], F. Sefkow[12], M. Seidel[13], R. Sell[12], A. Semenov[25], V. Shekelyan[12], I. Sheviakov[26], L.N. Shtarkov[26], G. Siegmon[17], U. Siewert[17], Y. Sirois[29], I.O. Skillicorn[11], P. Smirnov[26], J.R. Smith[8], V. Solochenko[25], Y. Soloviev[26], A. Specka[29], J. Spiekermann[9], S. Spielman[29], H. Spitzer[14], F. Squinabol[28], R. Starosta[1], M. Steenbock[14], P. Steffen[12], R. Steinberg[2], H. Steiner[12,40], B. Stella[33], J. Stier[12], J. Stiewe[16], U. Stößlein[36], K. Stolze[36], U. Straumann[38], W. Struczinski[2], J.P. Sutton[4], S. Tapprogge[16], M. Taševský[32], V. Tchernyshov[25], S. Tchetchelnitski[25], J. Theissen[2], C. Thiebaux[29], G. Thompson[21], P. Truöl[38], J. Turnau[7], J. Tutas[15], P. Uelkes[2], A. Usik[26], S. Valkár[32], A. Valkárová[32], C. Vallée[24], D. Vandenplas[29], P. Van Esch[5], P. Van Mechelen[5], Y. Vazdik[26], P. Verrecchia[10], G. Villet[10], K. Wacker[9], A. Wagener[2], M. Wagener[34], A. Walther[9], B. Waugh[23], G. Weber[14], M. Weber[12], D. Wegener[9], A. Wegner[27], H.P. Wellisch[27], L.R. West[4], T. Wilksen[12], S. Willard[8], M. Winde[36], G.-G. Winter[12], C. Wittek[14], E. Wünsch[12], J. Žáček[32], D. Zarbock[13], Z. Zhang[28], A. Zhokin[25], M. Zimmer[12], F. Zomer[28], J. Zsembery[10], K. Zuber[16], and M. zurNedden[38]

[1] I. Physikalisches Institut der RWTH, Aachen, Germany[a]
[2] III. Physikalisches Institut der RWTH, Aachen, Germany[a]
[3] Institut für Physik, Humboldt-Universität, Berlin, Germany[a]
[4] School of Physics and Space Research, University of Birmingham, Birmingham, UK[b]
[5] Inter-University Institute for High Energies ULB-VUB, Brussels; Universitaire Instelling Antwerpen, Wilrijk; Belgium[c]
[6] Rutherford Appleton Laboratory, Chilton, Didcot, UK[b]
[7] Institute for Nuclear Physics, Cracow, Poland[d]
[8] Physics Department and IIRPA, University of California, Davis, California, USA[e]
[9] Institut für Physik, Universität Dortmund, Dortmund, Germany[a]
[10] CEA, DSM/DAPNIA, CE-Saclay, Gif-sur-Yvette, France
[11] Department of Physics and Astronomy, University of Glasgow, Glasgow, UK[b]
[12] DESY, Hamburg, Germany[a]
[13] I. Institut für Experimentalphysik, Universität Hamburg, Hamburg, Germany[a]
[14] II. Institut für Experimentalphysik, Universität Hamburg, Hamburg, Germany[a]
[15] Physikalisches Institut, Universität Heidelberg, Heidelberg, Germany[a]
[16] Institut für Hochenergiephysik, Universität Heidelberg, Heidelberg, Germany[a]
[17] Institut für Reine und Angewandte Kernphysik, Universität Kiel, Kiel, Germany[a]
[18] Institute of Experimental Physics, Slovak Academy of Sciences, Košice, Slovak Republic[f]
[19] School of Physics and Chemistry, University of Lancaster, Lancaster, UK[b]
[20] Department of Physics, University of Liverpool, Liverpool, UK[b]

[21] Queen Mary and Westfield College, London, UK[b]
[22] Physics Department, University of Lund, Lund, Sweden[g]
[23] Physics Department, University of Manchester, Manchester, UK[b]
[24] CPPM, Université d'Aix-Marseille II, IN2P3-CNRS, Marseille, France
[25] Institute for Theoretical and Experimental Physics, Moscow, Russia
[26] Lebedev Physical Institute, Moscow, Russia[f]
[27] Max-Planck-Institut für Physik, München, Germany[a]
[28] LAL, Université de Paris-Sud, IN2P3-CNRS, Orsay, France
[29] LPNHE, Ecole Polytechnique, IN2P3-CNRS, Palaiseau, France
[30] LPNHE, Universités Paris VI and VII, IN2P3-CNRS, Paris, France
[31] Institute of Physics, Czech Academy of Sciences, Praha, Czech Republic[f,h]
[32] Nuclear Center, Charles University, Praha, Czech Republic[f,h]
[33] INFN Roma and Dipartimento di Fisica, Universita "La Sapienza", Roma, Italy
[34] Paul Scherrer Institut, Villigen, Switzerland
[35] Fachbereich Physik, Bergische Universität Gesamthochschule Wuppertal, Wuppertal, Germany[a]
[36] DESY, Institut für Hochenergiephysik, Zeuthen, Germany[a]
[37] Institut für Teilchenphysik, ETH, Zürich, Switzerland[i]
[38] Physik-Institut der Universität Zürich, Zürich, Switzerland[i]
[39] Visitor from Yerevan Phys. Inst., Armenia
[40] On leave from LBL, Berkeley, USA

[a] Supported by the Bundesministerium für Forschung und Technologie, FRG under contract numbers 6AC17P, 6AC47P, 6DO57I, 6HH17P, 6HH27I, 6HD17I, 6HD27I, 6KI17P, 6MP17I, and 6WT87P

[b] Supported by the UK Particle Physics and Astronomy Research Council, and formerly by the UK Science and Engineering Research Council

[c] Supported by FNRS-NFWO, IISN-IIKW

[d] Supported by the Polish State Committee for Scientific Research, grant Nos. SPUB/P3/202/94 and 2 PO3B 237 08, and Stiftung fuer Deutsch-Polnische Zusammenarbeit, project no.506/92

[e] Supported in part by USDOE grant DE F603 91ER40674

[f] Supported by the Deutsche Forschungsgemeinschaft

[g] Supported by the Swedish Natural Science Research Council

[h] Supported by GA ČR, grant no. 202/93/2423, GA AV ČR, grant no. 19095 and GA UK, grant no. 342

[i] Supported by the Swiss National Science Foundation

1 Introduction

The photon, exhibiting both point-like and hadronic behaviour, has a rich structure that is still not yet fully explored. New opportunities for studying photon interactions are opened by the HERA electron-proton collider. The nearly real photons produced by HERA's electron beam extend the energy range for photoproduction processes by more than one order of magnitude, up to the equivalent of tens of TeV in fixed target experiments, providing a large kinematic range for studying the properties of the photon. The H1 and ZEUS collaborations have begun to explore this domain, e.g. with measurements of the total γp cross section [1, 2, 3] and vector meson production [2, 4, 5, 6, 7].

In this paper we report the H1 results for the elastic ρ^0 photoproduction cross section at two average total energies, $\langle W_{\gamma p}\rangle = 55$ and 187 GeV, of the γp centre-of-mass system (cms). For the low energy measurement the associated differential cross sections, $\mathrm{d}\sigma/\mathrm{d}M_{\pi\pi}$, where $M_{\pi\pi}$ is the invariant mass of the ρ^0 decay products, $\mathrm{d}\sigma/\mathrm{d}t$, where t is the square of the four-momentum transfer at the proton vertex, and the polar decay angle distribution, $\mathrm{d}\sigma/\mathrm{d}\cos\theta^*$, of the ρ^0 are also presented.

At lower energies the photon is known to exhibit behaviour resembling that of a hadron. In particular, the reaction

$$\gamma + p \to \rho^0 + p \tag{1}$$

at cms energies of 10-20 GeV behaves much like elastic scattering of hadrons: the cross section is roughly constant with cms energy, the dependence on t of $\mathrm{d}\sigma/\mathrm{d}t$ is close to exponential and s-channel helicity conservation holds (the ρ^0 retains the helicity of the photon). This is interpreted in the Vector Meson Dominance (VMD) model [8, 9] as the fluctuation of the photon into a virtual ρ^0 meson, with subsequent elastic scattering of the ρ^0 on the proton. Regge theory [10] inspired models have been used successfully to describe the energy variation of the total cross section, with a 'soft' pomeron term dominating at high energies [11]. Models based on perturbative quantum chromodynamics (pQCD) may combine a soft VMD component with perturbatively calculable components to arrive at a total γp cross section. The $\gamma p \to \rho^0 p$ cross section may then be completely determined by the parameters used to fit the total γp cross section. Thus studies of reaction (1) at HERA energies help to constrain such models, as well as to clarify the nature of the pomeron. Thorough exploration of these interactions in the HERA energy regime is important for an eventual understanding of the hadronic properties of the photon.

Almost real photons, radiated at small angles by HERA's electron beam (26.7 GeV electrons in 1993 and 27.5 GeV positrons[1] in 1994), can interact with the 820 GeV protons at very high energies in the γp cms. In the VMD model, one expects dominant production of the vector meson series ρ^0, ω, ϕ along with other hadronic production. Elastic $\rho^0 p$ interactions are characterised by a scattering of the virtual ρ^0 meson and the proton at low $|t|$, leading to a ρ^0 at low p_t relative to the HERA beam axis. The ρ^0 subsequently decays into a $\pi^+\pi^-$ pair.

The kinematic variables are defined as follows:

$$\begin{aligned}
Q^2 &= -(k-k')^2 = -q^2 \\
t &= (q-v)^2 = (P-P')^2 \\
y &= \frac{q\cdot P}{k\cdot P} \\
s &= (P+k)^2 \\
W_{\gamma p} &= \sqrt{ys}
\end{aligned}$$

where y is the inelasticity parameter, Q^2 is the negative square of the four-momentum transfer at the electron vertex, $k(k')$ denotes the four vector of the incoming (scattered) electron, $P(P')$ of the incoming (scattered) proton, q of the photon and v of the vector meson.

[1]The term 'electron' will subsequently be used to refer to both electrons and positrons.

The two measurements presented in this paper were made under very different experimental conditions. In the low $W_{\gamma p}$ analysis, where the ρ^0 rest frame is boosted by about 1 unit of rapidity toward the electron beam direction, the ρ^0 decay products were observed in the central tracking detector (see section 2 for details of the H1 detector), enabling good reconstruction of the hadronic final state (excluding the proton, unseen in both analyses). The $W_{\gamma p}$ range ($40 < W_{\gamma p} < 80$ GeV) is, however, too low for the scattered electron to be detected in the small angle electron tagger. The kinematic quantities were therefore reconstructed from the ρ^0's two decay pions, using the assumptions of an elastic interaction and of $Q^2 = 0$ GeV^2. The resonant contribution to the cross section is deduced from the analysis of the line shape.

The high $W_{\gamma p}$ analysis used those data with an electron tag so that the $W_{\gamma p}$ range was $164 < W_{\gamma p} < 212$ GeV. At these high values of $W_{\gamma p}$ the ρ^0 rest frame is boosted by about 3 units of rapidity toward the electron beam direction and the decay products are kinematically forced outside the acceptance region of the tracking detectors, requiring reconstruction of the hadronic final state in the calorimeters. Since the spatial and energy resolutions of the calorimeters are worse than those of the trackers no measurement was possible of the resonance line shape, t dependence, or polar decay angle distribution.

The measured ep cross section is converted into a γp cross section, averaged over the available $W_{\gamma p}$ and Q^2 range so that $\langle\sigma_{\gamma p}\rangle = \int \frac{\mathrm{d}^2\sigma_{ep}}{\mathrm{d}y\mathrm{d}Q^2}\,\mathrm{d}y\mathrm{d}Q^2 / \int \Phi(y,Q^2)\,\mathrm{d}y\mathrm{d}Q^2$. In order to evaluate the photon flux, $\Phi(y,Q^2)$, we ignore any lepton beam polarisation and the longitudinal (helicity zero) contribution is neglected. In this case the flux for transverse virtual photons is given by the Weizsäcker-Williams approximation which we take in the form:

$$\Phi\left(y,Q^2\right) = \frac{\alpha}{2\pi Q^2}\left(\frac{1+(1-y)^2}{y} - \frac{2(1-y)}{y}\cdot\frac{Q^2_{\min}}{Q^2}\right) \quad ; \quad Q^2_{\min} = \frac{m_e^2 y^2}{1-y}, \qquad (2)$$

where α is the fine structure constant and m_e is the electron mass [12, 13]. The quantity $Q^2_{\min}$ is the minimum photon virtuality which is kinematically allowed. The upper limit on the Q^2 range over which the measurements were taken, $Q^2_{\max}$, is determined by the experimental procedure used. For the low $W_{\gamma p}$ analysis the requirement of $|t_{\mathrm{rec}}| < 0.5$ GeV^2 (see section 4) implies effectively $Q^2_{\max} \approx 0.5$ GeV^2 and the mean Q^2 is $\langle Q^2\rangle = 0.035$ GeV^2. The requirement of the scattered electron to be detected in the tagger in the high $W_{\gamma p}$ analysis gives $Q^2_{\max} \approx 0.01$ GeV^2 and $\langle Q^2\rangle = 0.001$ GeV^2.

With an assumption for the Q^2 dependence of the virtual photon-proton cross section, the total elastic ρ^0 cross section at $Q^2 = 0$ may be extrapolated from $\langle\sigma_{\gamma p}\rangle$. In a VMD model [8] in which the ρ^0 dominates, the longitudinal and transverse virtual photon-proton cross sections are related by $\sigma^L_{\gamma^* p} = \sigma^T_{\gamma^* p}\cdot Q^2/M^2_\rho$ and evolve such that $\sigma^T_{\gamma^* p} \propto 1/(1+Q^2/M^2_\rho)^2$. With these assumptions, corrections averaged over the selected samples of events amount to +3.9 % and +0.2 % for the low and high $W_{\gamma p}$ analyses respectively. All results quoted in this paper do not include any correction for this extrapolation.

2 The H1 Detector

A complete description of the detector is available elsewhere [14]. Only a brief description of the parts of the detector relevant to these analyses is included here. In H1 the z-axis points in the proton beam direction, denoted by the term 'forward'.

The H1 Central Tracking Detector (CTD) provides charged track measurement and triggering in the pseudorapidity ($\eta = -\ln\tan\theta/2$) range $-1.5 < \eta < 1.5$. Its main components are two concentric drift chambers, Central Jet Chambers 1 and 2 (CJC1 and CJC2). Located at the inner radius of CJC1 and CJC2 are two sets of cylindrical drift chambers for measurement of the z-coordinate and two proportional chambers, CIP and COP. The entire CTD is situated within a 1.15 T solenoidal magnetic field, parallel to the proton beam axis. The transverse momentum resolution for charged tracks is $\sigma(p_t)/p_t \approx 0.009 \cdot p_t(\mathrm{GeV}) \oplus 0.015$. The CTD was the detector used to trigger and reconstruct the two particle hadronic final state in the low $W_{\gamma p}$ analysis.

The CTD is surrounded by a finely segmented Liquid Argon calorimeter (LAr) that provides hadronic and electromagnetic energy measurements in the range $-1.5 < \eta < 3.3$. Instrumented sections of the return yoke of the magnet outside the LAr calorimeter provide tracking and hadronic 'tail-catching' calorimetry in the range $-2.5 < \eta < 3.4$. These detectors were used to veto inelastic and cosmic muon events.

In the forward region two detectors were used to veto proton dissociation events: the forward muon detector (FMD) and the proton remnant tagger (PRT). They were used in the high $W_{\gamma p}$ analysis to tag hadrons produced at large values of pseudorapidity ($5.0 < \eta < 7.5$) by detecting secondary particles issued from collisions with the beam pipe or adjacent material. The FMD consists of planes of drift chambers at $6 < z < 9$ m and the PRT is made up of scintillator planes at $z = 24$ m.

Two detectors provide coverage in the backward direction. The Backward Electromagnetic Calorimeter (BEMC), a lead scintillator calorimeter covering the range $-3.4 < \eta < -1.5$, was used to reconstruct the hadronic final state in the high $W_{\gamma p}$ analysis, while the Backward Proportional Chamber (BPC), $-3.0 < \eta < -1.5$, helped in the rejection of beam-gas background.

Behind the BEMC are located the Time of Flight (ToF) scintillator walls, covering a pseudorapidity range of $-3.5 < \eta < -2.0$. Their timing information was used to reject background upstream proton interactions and in the high $W_{\gamma p}$ analysis as a trigger.

The luminosity system, monitoring the reaction $ep \to e\gamma p$, consists of two TlCl/TlBr crystal calorimeters. The electron tagger is located at $z = -33$ m and the photon detector at $z = -103$ m. The electron tagger was also used to detect and trigger on the scattered electron for the high $W_{\gamma p}$ analysis.

3 Monte Carlo

Two Monte Carlo (MC) generators were used in these analyses, PYTHIA [15] and PHOJET [16]. Five MC photoproduction mechanisms are distinguished: elastic interactions (EL) which describe $\gamma p \to Vp$ where V stands for one of the vector mesons ρ^0, ω or ϕ, single photon diffractive dissociation (GD) in which the photon dissociates ($\gamma p \to Xp$), single proton diffractive dissociation (PD) in which the proton dissociates ($\gamma p \to VY$), double diffractive dissociation (DD) in which both photon and proton dissociate ($\gamma p \to XY$) and non-diffractive interactions (ND). This last category includes all reactions not included in the previous classes. The ratios of the cross sections for the 5 processes were chosen following comparisons made using the high $W_{\gamma p}$ data (see section 5) and the constraint imposed by the measurement made of the total $W_{\gamma p}$ cross section [3]:

$$\sigma_{\mathrm{EL}} : \sigma_{\mathrm{GD}} : \sigma_{\mathrm{PD}} : \sigma_{\mathrm{DD}} : \sigma_{\mathrm{ND}} = 1 : 1.25 : 0.75 : 2.00 : 5.0\,. \tag{3}$$

All channels were generated with a Q^2 dependence following equation 2 with no dependence on $W_{\gamma p}$ for the photon-proton cross section.

Both MC generators have similar inputs for the EL channel. Events are generated with a t-dependence of e^{bt} where $b \approx 11$ GeV^{-2}, a decay angular distribution in the ρ^0 rest frame $\cos\theta^*$ proportional to $\sin^2\theta^*$, as expected for a transversely polarised ρ^0 (helicity ± 1), and a skewed mass distribution consistent with that measured (see section 6). The relative rates of ρ^0, ω and ϕ production were chosen to be 13:1.5:1 following measurements made at lower energies [9].

For the singly diffractive dissociation channels (GD, PD) PYTHIA assumes a t-dependence of $b \approx 5$ GeV^{-2}. PHOJET assumes a b parameter that depends on the mass of the diffractive system, M_X, so that $b \approx 11$ GeV^{-2} at $M_X = M_\rho$ and becomes smaller for higher M_X [17]. For the double diffractive dissociation and for both MC generators, $b \approx 2 - 3$ GeV^{-2}.

Diffractive dissociation of the proton or photon is described in PYTHIA according to a distribution such that roughly $\mathrm{d}N/\mathrm{d}M_X^2 \sim 1/M_X^2$ with an enhancement at lower masses. Masses are generated starting at 0.2 GeV (twice the pion mass) above the mass, M_{in}, of the incoming particle, with the ρ^0 mass used for the incoming γ. PHOJET in contrast generates a mass spectrum according to $\mathrm{d}N/\mathrm{d}M_X^2 \sim 1/(M_X^2 - M_{in}^2)$ at higher masses and treats the lower part as a single resonance. The spectrum starts at twice the pion mass above M_{in}.

The MC event samples included a full simulation of the H1 detector and were subject to the same reconstruction as each of the two data samples.

4 The Low $W_{\gamma p}$ Analysis

The data for this analysis were taken in 1993 when HERA operated with 90 bunches of 820 GeV protons and 94 bunches of 26.7 GeV electrons with 84 colliding bunch pairs. A small number of non-colliding electron and proton bunches, called 'pilot' bunches, were included in order to estimate the beam-gas background. The data sample was limited to the largest continuous segment of runs containing stable and uniform central tracker conditions and amounted to a total integrated luminosity of 19.8 ± 1.0 nb^{-1}.

The most favourable trigger capable of distinguishing the soft, low multiplicity hadronic final state from the high level of background was the Drift Chamber r-ϕ trigger (DCRϕ) which distinguished individual tracks by matching CJC1 and CJC2 wire hits with predefined masks [18]. The major drawback to this trigger was that its efficiency threshold, at $p_t \approx 450$ MeV, was located above the peak of the decay pion p_t distribution. It was found that the best trigger condition required one and only one track pattern identification by the DCRϕ. A requirement of two (or more) tracks above the threshold would have severely reduced the trigger efficiency and resulted in an unacceptable rate of background triggers. Thus, the second track in the event would usually have a p_t below threshold and would not be detected by the trigger. In order to reduce the rate of beam-gas triggers, the overall trigger required in addition a single vertex reconstruction by CIP and COP [19] (z-vertex) and was vetoed if there was significant energy present in the forward part of LAr, excessive activity in the backward portion of CIP or an out-of-time ToF signal indicating a background event.

Approximately 1.4×10^5 events satisfied the trigger. Analysis of the data from the pilot bunches indicated that the vast majority of triggered events consisted of proton beam induced background. The data were reduced in a three stage procedure consisting of computer selections and a visual scan.

Since this analysis relies on the identification of the two particle final state, it is particularly sensitive to the quality of track reconstruction. Having observed differences between the data and MC track multiplicities, a visual scan early in the analysis was found to be necessary in order to establish equivalent data and MC samples of clean two particle events. This procedure also allowed a measurement of the event reconstruction efficiency independent of the MC simulation.

The first stage in data reduction employed a loose track requirement which was essentially independent of track reconstruction quality. Its purpose was to eliminate the obvious events that were not composed of only two particles, thereby reducing the data sample to a manageable size for scanning. Those events with a total of 1 track and no other track segments, 2 like sign, or more than 3 well reconstructed tracks were rejected. All other events were kept. A sub-sample of 600 of the rejected events were scanned and only one event was incorrectly rejected due to an improper track reconstruction (a 0.3 % error).

The reduced sample of $\approx 47 \times 10^3$ events was then scanned using the H1 event display program. Each event was required to have two opposite sign track patterns pointing to a common vertex and extending radially out to at least CJC2 ($r \gtrsim 43$ cm). Only digitised hit information from the CJC detectors was used in the scan. Obvious cosmic events with tracks in the muon detector were removed. A total of 12,200 valid two-particle, opposite-sign events passed the scan including 623 from the proton pilot bunch crossings and 13 from the electron pilot bunch crossings.

Using the track fitting of the standard H1 reconstruction program, the third stage of the reduction focussed on filtering two-particle events with well-reconstructed vertices. The efficiencies for data and MC events to pass this stage in the analysis were found to be $0.8430 \pm 0.0034\,(\mathrm{stat.})$ and $0.8807 \pm 0.0022\,(\mathrm{stat.})$, respectively. The ratio of the data to MC efficiencies was used as a correction factor to account for this remaining difference in event reconstruction (C in equation 5).

An accurate reconstruction of kinematic variables was possible using only the reconstructed ρ^0 and the assumption of an elastic event with $Q^2 = 0$ GeV^2. Figures 1a and 1b compare the reconstructed to the generated values for $W_{\gamma p}$ and t. The mean differences were not significant: $\Delta W_{\gamma p} \approx 0.4$ GeV with an RMS of 1.2 GeV, $\Delta t \approx 0.0$ GeV^2 with an RMS of 0.02 GeV^2.

The final set of filters uses kinematic cuts to reduce the number of background events. Each event was required to have:

- a total energy in the forward, inner part of the LAr calorimeter ($1.7 < \eta < 3.3$), of less than 400 MeV suppressing events in which the proton dissociates,

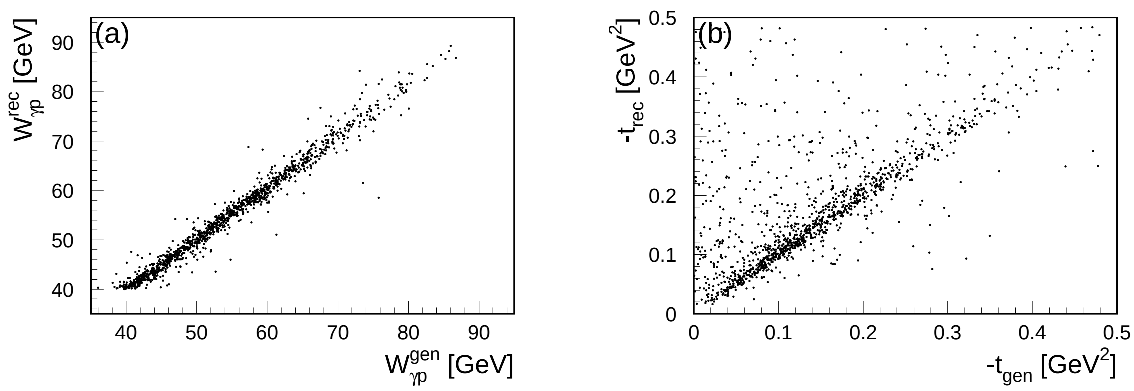

Figure 1: (a) MC reconstructed versus generated $W_{\gamma p}$; (b) MC reconstructed versus generated t for the low $W_{\gamma p}$ analysis. Only elastic ρ^0 events are shown. The distributions are shown after all cuts were applied.

- $p_t > 0.5$ GeV for the high p_t track and $p_t < 0.4$ GeV for the low p_t track, matching the region of flat efficiency in p_t for the DCRϕ trigger,
- $|t_{\rm rec}| < 0.5$ GeV^2, with $t_{\rm rec} = -p_t^{\pi\pi}$ being the reconstructed t, reducing the number of dissociative and inelastic events,
- $W_{\gamma p}^{\rm rec} > 40$ GeV, cutting most of the proton beam-gas events present in data and restraining the measurement to the range where there is reasonable acceptance,
- $M_{\pi\pi} \in [0.52, 1.17]$ GeV, limiting the measurement to the range where there is a reasonable signal to background ratio.

A total of 358 colliding bunch events and no pilot events survive all cuts.

The trigger efficiency was measured using independent samples of events, where there was a chance overlap between the reaction $ep \to e\rho^0 p$ and the Bethe-Heitler process $ep \to e\gamma p$. These events were triggered by the detection of the electron from the Bethe-Heitler process in accidental coincidence with a signal from other detector components. The LAr veto was found to be 100% efficient for the selected events. Triggers independent of the CTD were used to determine the z-vertex efficiency $\epsilon_{z-\rm vertex}$. With slightly relaxed selection criteria, $\epsilon_{z-\rm vertex} = 0.72 \pm 0.03(\rm stat.)$ was obtained, in agreement with MC simulations. The relative efficiency of the DCRϕ and remaining requirements for events already fulfilling the z-vertex trigger, $\epsilon_{\rm DCR\phi}$, was determined from a sample triggered by the electron and the z-vertex condition only. Applying the final selection procedure and cuts ensured the same event properties as for the signal sample and gave $\epsilon_{\rm DCR\phi} = 0.29 \pm 0.06(\rm stat.)$. The results were multiplied together to obtain the overall trigger efficiency of $\epsilon_{\rm trig} = 0.21 \pm 0.04$. The error quoted is dominated by the low statistics in the overlap sample.

Backgrounds in the final sample were estimated using the PYTHIA MC generator. Only the diffractive channels were found to contribute significantly. The estimated background fractions in the final sample of ρ^0 candidates was $13 \pm 7\,\%$ from GD, $9 \pm 5\,\%$ from PD, $10 \pm 5\,\%$ from DD, $0 \pm 1\,\%$ from ND and $1 \pm 1\,\%$ from elastic production of ω and ϕ mesons[2]. The errors on the background includes the uncertainty in the decomposition of the total photoproduction cross section.

Figure 2 shows the dipion mass spectra of the accepted data (without background subtraction) for the low $W_{\gamma p}$ analysis along with the MC prediction. The MC mass shape, containing a Ross-Stodolsky skewed mass distribution for the elastic ρ^0 events (see section 6.1 for details), matches the shape of the data histogram well.

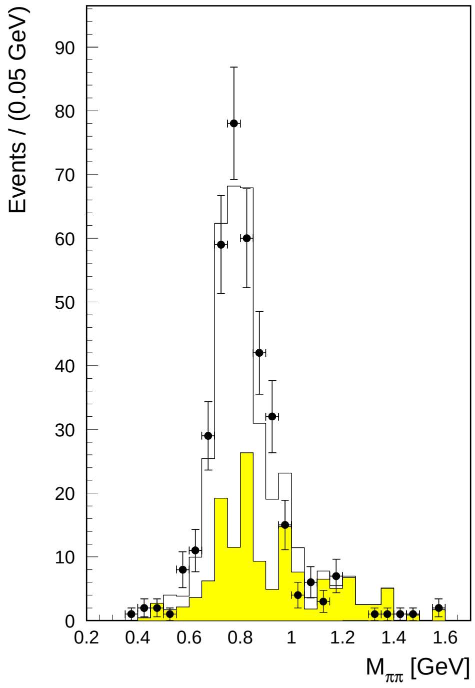

Figure 2: Reconstructed $M_{\pi\pi}$ distributions for the low $W_{\gamma p}$ data sample before background subtraction and acceptance correction. The open histogram shows the MC (PYTHIA) prediction for all possible channels (normalised to the data). The shaded histogram shows the MC prediction for all channels apart from EL.

5 The High $W_{\gamma p}$ Analysis

The data for this measurement were collected during a short dedicated run in the 1994 data taking period with a vertex shifted forward of its nominal position by ≈ 70 cm. With this vertex position the acceptance for particles travelling backwards at small angles to the beam pipe is enhanced. The HERA machine was operated with 153 colliding bunches of

[2]The p_t cuts imposed on the tracks strongly suppress events from the reaction $\gamma p \to \phi p$, $\phi \to K^+K^-$

27.5 GeV positrons and 820 GeV protons with in addition 17 proton and 15 positron pilot bunches. The data taken correspond to a total integrated luminosity of 23.8 ± 1.3 nb^{-1}.

Photoproduction events were triggered by the coincidence of a signal in the electron tagger ($E'_e > 4$ GeV) and a signal in the ToF system coming from the time interval expected for ep interactions. This trigger has been shown to have a high (35 %) and well understood acceptance for all photoproduction processes for data taken over a similar $W_{\gamma p}$ range [3].

The main source of background in the triggered sample was found to be electron beam interactions with residual gas or with material inside the beam pipe. This background was reduced by requiring at least one BPC hit and a total energy deposition greater than 0.2 GeV in the BEMC or LAr calorimeters. The measurement was further restricted to the kinematic range $0.3 < y < 0.5$ where there was good electron tagger acceptance.

Two classes of diffractive events were distinguished on the basis of a 'rapidity gap' i.e. a region of laboratory pseudorapidity where no particles are observed in the final state. The first, termed an elastic proton sample where in most cases the proton remained intact (GD and EL), was selected as follows. No activity was required above threshold in the forward detectors (FMD and PRT). The pseudorapidity, $\eta_{\max}$, of the most forward energy deposit greater than 600 MeV in the LAr or BEMC calorimeters or the most forward track in the CTD was required to be less than 3. The second class of event, where the proton dissociates (DD and PD), was selected by requiring there to be signals in either FMD, PRT or $\eta_{\max} > 3$. ND events in the proton dissociation sample were suppressed by requiring $\Delta\eta$, the largest region in the detector where no tracks or energy deposits were found, to be greater than 2 units of pseudorapidity with the upper edge of the rapidity gap having $\eta > 2.5$. It should be noted that these latter requirements also suppress those events where the proton fragments into a high mass system and in which the rapidity gap is small or non-existent. The distinction between these DD events and ND events is experimentally not well defined. Studies with the MC generator indicate that these cuts restrict the proton dissociation sample to a proton dissociation mass of $M_Y < 10$ GeV.

The four vector $(E_h, P_{xh}, P_{yh}, P_{zh})$ of the hadronic final state excluding the proton or the dissociative proton system was determined by combining calorimeter (LAr and BEMC) and tracking (CTD) information in a procedure that avoided double counting and optimised the resolution. For the proton dissociation sample, only those tracks/energy deposits at angles more backward of the rapidity gap were included. The reconstructed invariant mass of the hadronic final state excluding the proton, $M_X^{\rm rec}$, was then calculated making the assumption that $P_{xh}^2 + P_{yh}^2 \simeq |t| \ll (M_X^{rec})^2$ and using the approximation $y = (E_h - P_{zh})/(2E_e)$ so that

$$M_X^{\rm rec} = \sqrt{(E_h + P_{zh}) \cdot 2 \cdot E_e \cdot y}. \tag{4}$$

Here E_e is the electron beam momentum and y is reconstructed from the final state electron. This method resulted in good resolution, as demonstrated by figure 3, even though a significant proportion of the hadronic energy is not detected in the backward region. It should be noted, however, that the resolution width in $M_X^{\rm rec}$ is much greater than the width of the ρ^0 decay, making it impossible to determine the line shape with this analysis.

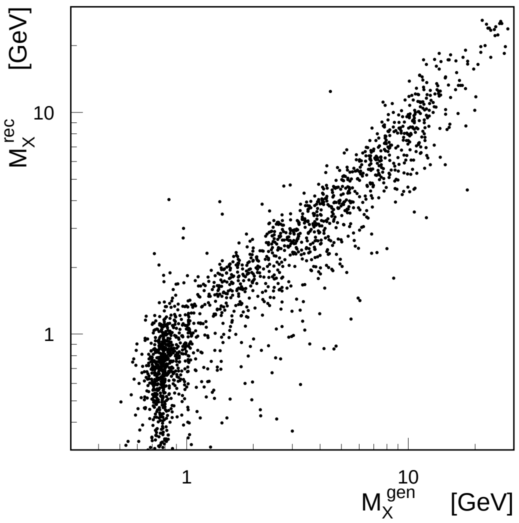

Figure 3: MC reconstructed versus generated M_X for the high $W_{\gamma p}$ analysis. All diffractive channels (EL, GD, DD, GD) are shown.

A sample of events where elastic ρ^0 production dominates was selected by requiring $0.4 < M_X < 1.26$ GeV in the elastic proton sample.

Background in the elastic ρ^0 sample was observed and attributed to four dominant sources: electron beam induced, GD, PD where none of the proton fragments were detected and EL from ω and ϕ production.

The electron beam induced background was estimated using pilot bunch events, was found to contribute $\approx 20 \pm 5\,\%$ and was removed from the sample.

The MC generators (PYTHIA and PHOJET) were used to estimate the fraction of GD, PD, EL, DD and ND background. The relative cross sections used in the generation for the four diffractive processes described above were chosen by comparison of the $M_X^{\rm rec}$ spectra in data and MC for both the elastic proton and proton dissociation samples. The region where $M_X^{\rm rec} > 1.26$ GeV was found to be dominated by GD and DD and that where $M_X^{\rm rec} < 1.26$ GeV by EL and PD. Since the relative cross sections obtained in this comparison for PYTHIA and PHOJET were in broad agreement, the same fractions were used for both MC generators (see equation 3). This choice also satisfied the constrains imposed in [3]. Figures 4 (a,b) show comparisons of the data with MC predictions (with the cross section ratios as described above) for the $M_X^{\rm rec}$ distributions of the elastic proton and dissociated proton samples. For these plots and subsequent results the average of the two MC generators was used.

The ratio of GD events produced in the MC generators for $0.4 < M_X^{\rm true} < 1.26$ GeV to EL events was found to be $\approx 6\,\%$. This number agrees well with measurements made at lower energies [20]. The GD, PD, EL, DD and ND background fractions in the elastic ρ^0 sample were estimated to be $12 \pm 6\,\%$, $6 \pm 3\,\%$, $10 \pm 5\,\%$, $3 \pm 2\,\%$ and $0 \pm 1\,\%$ respectively.

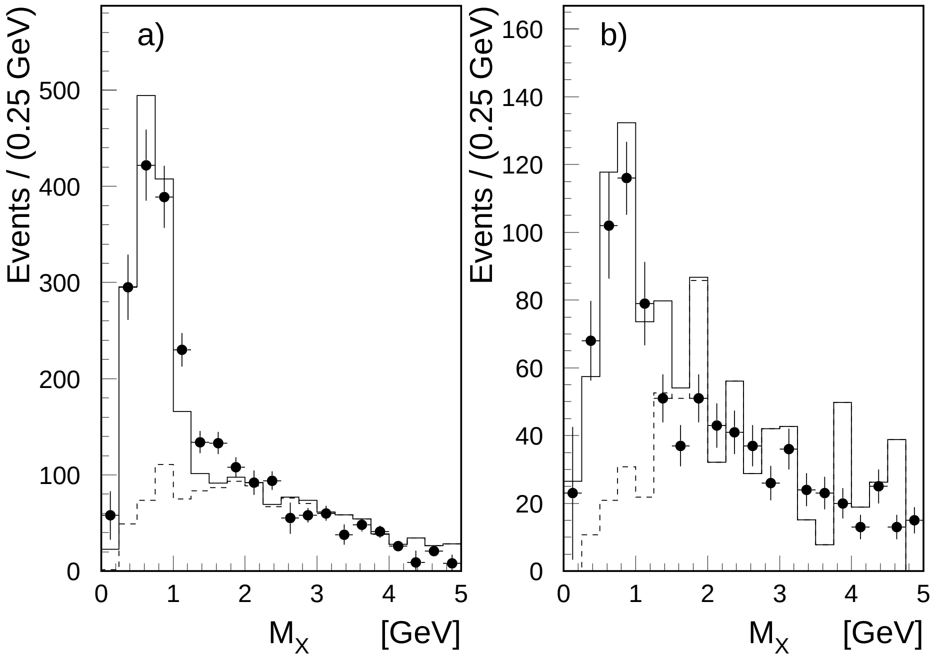

Figure 4: Reconstructed M_X distribution for the high $W_{\gamma p}$ data for a) the elastic proton selection and b) for the proton dissociation selection. The solid histograms show the MC prediction for all possible channels. The dashed histograms show the MC prediction for a) all channels apart from EL and b) all channels apart from PD. The MC distributions were normalised to the data in the region $M_X < 1.26$ GeV in the elastic proton selection.

As for the low $W_{\gamma p}$ case the errors on the background estimates accommodate the range of uncertainty in the decomposition of the total photoproduction cross section into its five constituent processes [3]. All backgrounds were subtracted statistically from the data.

The acceptance for the electron tagger and for the detection of the hadronic final state were determined separately. The first was determined in a procedure identical to that described in [3], was found to be 61 %. The hadronic final state acceptance was determined by taking the mean of the values obtained from two MC generators, namely 39 % and 40 % for PYTHIA and PHOJET respectively.

6 Results

6.1 The Differential $\pi^+\pi^-$ Cross Section $\mathrm{d}\sigma/\mathrm{d}M_{\pi\pi}$

The corrected differential cross section of the invariant mass of the $\pi^+\pi^-$ system, $\mathrm{d}\sigma/\mathrm{d}M_{\pi\pi}$, was determined for the data taken at $\langle W_{\gamma p}\rangle = 55$ GeV from the raw distribution (shown in figure 2) using

$$\frac{\mathrm{d}\sigma}{\mathrm{d}M_{\pi\pi}} = \frac{N_{\mathrm{bin}} - N_{\mathrm{bgd}}}{\Phi_I\,\mathcal{L}\,\varepsilon_{\mathrm{trig}}\,\varepsilon_{\mathrm{bin}}\,C} \cdot \frac{1}{1+R_{\mathrm{PD}}} \cdot \frac{1}{\Delta M}. \tag{5}$$

Here:

- N_{bin} is the number of events reconstructed in each mass bin,
- N_{bgd} is the estimated number of background events in the bin, from GD, DD, ND and EL,
- R_{PD} is the estimated ratio of PD to EL (taken as a constant scaling factor for all bins),
- Φ_I is the photon flux found by integration of equation 2, for $40 < W_{\gamma p} < 80$ GeV and $Q^2_{\mathrm{min}} < Q^2 \lesssim 0.5\ \mathrm{GeV}^2$,
- $\mathcal{L}$ is the integrated luminosity,
- $\varepsilon_{\mathrm{trig}}$ is the global trigger efficiency as calculated in section 4,
- $\varepsilon_{\mathrm{bin}}$ is the bin by bin selection efficiency given by the MC before the trigger selection, averaged over the kinematical range generated,
- C is the efficiency correction equal to the ratio of data to MC track reconstruction efficiencies,
- ΔM is the bin width.

The acceptance, $\varepsilon_{\mathrm{bin}}$, varied between 2 % and 37 % with an average value of 15 %. The integrated photon flux is $\Phi_I = 0.0621$. The production cross section is shown in figure 5. The mass dependence of $\mathrm{d}\sigma/\mathrm{d}M_{\pi\pi}$ is consistent with a large contribution from ρ^0 photoproduction. The peak is shifted to lower values than the nominal ρ^0 mass and there is an enhancement (suppression) of the cross section at values lower (higher) than the nominal ρ^0 mass. This asymmetric shape, or skew, of the distribution is a well known feature of ρ^0 photoproduction which can be attributed to an interference between the resonant and non-resonant production of two pions. In the phenomenological approach by Ross and Stodolsky [21] the differential cross section is assumed to follow

$$\frac{\mathrm{d}\sigma}{\mathrm{d}M_{\pi\pi}} = f_\rho \cdot BW_\rho(M_{\pi\pi}) \cdot (M_\rho/M_{\pi\pi})^{n_{\mathrm{RS}}} \tag{6}$$

where f_ρ and n_{RS} are constants and

$$BW_\rho(M_{\pi\pi}) = \frac{M_{\pi\pi} M_\rho \Gamma_\rho(M_{\pi\pi})}{(M_\rho^2 - M_{\pi\pi}^2)^2 + M_\rho^2 \Gamma_\rho^2(M_{\pi\pi})}, \tag{7}$$

where M_ρ is the ρ^0 mass and where the momentum dependent width, following the suggestion of Jackson [22], is taken to be

$$\Gamma_\rho(M_{\pi\pi}) = \Gamma_0 (\frac{q^*}{q_0^*})^3 \frac{2}{1+(q^*/q_0^*)^2}. \tag{8}$$

Here Γ_0 is the ρ^0 width, q^* is the π momentum in the $\pi^+\pi^-$ rest frame and q_0^* is the value of q^* when $M_{\pi\pi} = M_\rho$. The distortion of the mass spectrum is characterised by the Ross-Stodolsky parameter n_{RS}, which becomes zero for production of just the resonance.

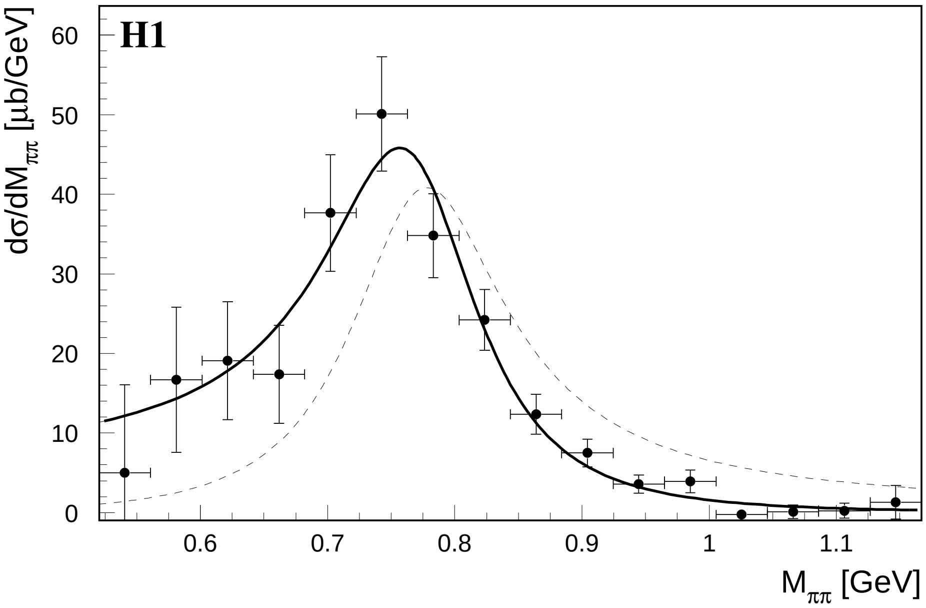

Figure 5: The $\mathrm{d}\sigma/\mathrm{d}M_{\pi\pi}$ distribution at $\langle W_{\gamma p}\rangle = 55$ GeV for $|t| < 0.5$ GeV^2. Only statistical errors are shown. The solid curve represents a fit to the distribution assuming the parameterisation of Ross and Stodolsky (equations 7 and 9). The dashed curve shows the pure Breit Wigner (equation 7 with $n_{\mathrm{RS}} = 0$).

The spectrum was fitted, using the parameterisation of equation 6, over the range $0.52 < M_{\pi\pi} < 1.17$ GeV with quantities f_ρ, M_ρ, Γ_0 and n_{RS} left as free parameters. The fit is shown in figure 5 and the results are summarised in table 1. The values of M_ρ and Γ_0 are in agreement with particle data group (PDG) values of $M_\rho = 769.9 \pm 0.8$ MeV and $\Gamma_0 = 151.2 \pm 1.2$ MeV [23]. The value of the differential cross section at the nominal ρ^0 mass was measured to be

$$\left.\frac{\mathrm{d}\sigma}{\mathrm{d}M_{\pi\pi}}\right|_{M_{\pi\pi}=M_\rho} = 44 \pm 5\,(\mathrm{stat.}) \pm 12\,(\mathrm{syst.})\;\mu\mathrm{b\,GeV}^{-1}.$$

The systematic error was determined in a similar way to that described in section 6.2. Spital and Yennie have suggested that the value of the differential cross section at the nominal ρ^0 mass offers a way to determine the total elastic ρ^0 cross section independently of the assumptions made for the form of the line shape since it is at the nominal ρ^0 mass where there is little or no interference of any additional coherent production [24]. With their assumption of a standard Breit Wigner for the ρ^0 resonance line shape, we get

$$\sigma(\gamma p \to \rho^0 p) = \frac{\pi\Gamma_0}{2}\left.\frac{\mathrm{d}\sigma}{\mathrm{d}M_{\pi\pi}}\right|_{M_{\pi\pi}=M_\rho} = 10.6 \pm 1.1(\mathrm{stat.}) \pm 3.0(\mathrm{syst.})\;\mu\mathrm{b}$$

Parameter	Value			
M_ρ	783	$\pm$	13	MeV
Γ_0	153	$\pm$	19	MeV
f_ρ	6.23	$\pm$	0.62	μb
n_{RS}	5.84	$\pm$	1.05	
χ^2/ndf	12.81/12			

Table 1: Results of the fit of the $\mathrm{d}\sigma/\mathrm{d}M_{\pi\pi}$ distribution for $\langle W_{\gamma p}\rangle = 55$ GeV and $|t| < 0.5$ GeV^2 assuming a Ross-Stodolsky skewing factor (see text). The errors shown are statistical.

In order to investigate the sensitivity of the results to changes in the assumed parameterisation of the mass spectrum, the data were reanalysed with a fit based on the Söding interference model [25] and with different assumptions for the momentum dependent width. In the Söding model the skewing of the mass spectrum is explained by the interference of a resonant $\rho^0 \to \pi^+\pi^-$ amplitude and a p-wave $\pi\pi$ Drell type background term [26]. A simplified parameterisation of the model used in [6, 27] can be written as

$$\frac{\mathrm{d}\sigma}{\mathrm{d}M_{\pi\pi}} = f_\rho \cdot BW_\rho(M_{\pi\pi}) + f_I \cdot I(M_{\pi\pi}), \tag{9}$$

where $BW_\rho(M_{\pi\pi})$ is defined in equation 7 and the interference term is

$$I(M_{\pi\pi}) = \frac{M_\rho^2 - M_{\pi\pi}^2}{(M_\rho^2 - M_{\pi\pi}^2)^2 + M_\rho^2\Gamma_\rho^2(M_{\pi\pi})}. \tag{10}$$

The quantities f_ρ, f_I, M_ρ and Γ_0 are left as free parameters. The fit was also done for both models with the following two parameterisations of the momentum dependent width, used by some other experiments [27, 28, 29]

$$\Gamma_\rho(M_{\pi\pi}) = \Gamma_0(\frac{q^*}{q_0^*})^3, \tag{11}$$

$$\Gamma_\rho(M_{\pi\pi}) = \Gamma_0(\frac{q^*}{q_0^*})^3\frac{M_\rho}{M_{\pi\pi}} \tag{12}$$

The results of the fits are summarised in table 2. All of the fits yielded values for M_ρ and Γ_0 in agreement apart from that using the Söding model with the width of equation 11.

6.2 The Elastic ρ^0 Photoproduction Cross Section

The $\gamma p \to \pi^+\pi^- p$ cross section at $\langle W_{\gamma p}\rangle = 55$ GeV was obtained by integrating the fitted form of the differential invariant mass spectrum of equation 6 with a momentum dependent width as in equation 8. This procedure involves an extrapolation outside the measured region, $0.52 < M_{\pi\pi} < 1.17$ GeV, to the region $2M_\pi < M_{\pi\pi} < M_{\text{cut}}$, where, following the procedure used by [6], the upper mass limit is taken to be $M_{\text{cut}} = M_\rho + 5\Gamma_0$. In making

Model	χ^2/ndf	M_ρ /MeV	Γ_0 /MeV	f_ρ /μb	n_{RS}	f_I /μbGeV^{-1}
RS +(8)	1.07	783 ± 13	153 ± 19	6.23 ± 0.62	5.84 ± 1.05	—
RS +(11)	1.09	791 ± 14	163 ± 23	6.11 ± 0.65	6.84 ± 1.00	—
RS +(12)	1.09	784 ± 13	153 ± 19	6.20 ± 0.62	5.95 ± 1.01	—
S +(8)	0.84	787 ± 12	176 ± 28	6.70 ± 0.55	—	3.39 ± 0.85
S +(11)	1.02	815 ± 16	205 ± 40	5.86 ± 0.49	—	5.07 ± 1.20
S +(12)	0.88	793 ± 13	181 ± 30	6.57 ± 0.54	—	3.74 ± 0.92

Table 2: The results of the fits of the $\mathrm{d}\sigma/\mathrm{d}M_{\pi\pi}$ spectrum for the low $W_{\gamma p}$ analysis. In the column marked 'Model': RS is the Ross-Stodolsky parameterisation of equation 6, S is the Söding parameterisation of equation 9. The bracketed numbers refer to the equation describing the momentum dependent width. The errors quoted are only statistical. The column labels are specified in the text.

the extrapolation we assume a t dependence with a slope parameter $b = 10.9$ GeV^{-2}, as obtained from the fit of the $\mathrm{d}\sigma/\mathrm{d}t$ distribution in section 6.3, so that

$$\frac{\mathrm{d}^2\sigma(\gamma p \to \pi^+\pi^- p)}{\mathrm{d}M_{\pi\pi}\,\mathrm{d}t} = A(M_{\pi\pi}) \cdot e^{bt}. \tag{13}$$

The integration is performed over the limits -0.5 GeV$^2 < t < t_{\mathrm{min}}$, where $|t_{\mathrm{min}}|$ is the minimum value of $|t|$ which is kinematically allowed. The fraction of the cross section that lies outside the measured kinematic region in $M_{\pi\pi}$, ξ, is found to be $\xi = 0.15$. The resulting total $\gamma p \to \pi^+\pi^- p$ cross section is

$$\sigma(\gamma p \to \pi^+\pi^- p) \quad = \quad 11.2 \pm 1.1\,(\mathrm{stat.}) \pm 3.1\,(\mathrm{syst.})\ \mu\mathrm{b}.$$

The resonant part of the total cross section is obtained by integrating the function $f_\rho \cdot BW_\rho(M_{\pi\pi})$ (i.e. taking $n_{\mathrm{RS}} = 0$ in equation 6), assuming the same t dependence as before, over the prescribed range in $M_{\pi\pi}$. The value of the cross section, measured at $\langle W_{\gamma p}\rangle = 55$ GeV for $2M_\pi < M_{\pi\pi} < M_\rho + 5\Gamma_0$ and -0.5 GeV$^2 < t < t_{\mathrm{min}}$ is then

$$\sigma(\gamma p \to \rho^0 p) \quad = \quad 9.1 \pm 0.9\,(\mathrm{stat.}) \pm 2.5\,(\mathrm{syst.})\ \mu\mathrm{b}.$$

At the present level of experimental precision there are no corrections to be made for ρ^0 decay modes other than to $\pi^+\pi^-$.

For the chosen value of $M_{\mathrm{cut}} = M_\rho + 5\Gamma_0$ the extracted cross section, $\sigma(\gamma p \to \rho^0 p)$, was found to be very stable against changes in the parameterisation of the $\mathrm{d}\sigma/\mathrm{d}M_{\pi\pi}$ spectrum. Allowing n_{RS} to vary within the statistical errors resulted in a change of $\pm 6.0\,\%$. Repeating the fit with values for M_ρ and Γ_0 fixed to the PDG values gave an increase of 7.0 %. Using the parameterisation of equation 9 gave an increase of the cross section of 5.9 % and the maximum variation caused by different assumptions of the momentum dependence of the width was 6.6 %.

If, however, we do not impose an upper $M_{\pi\pi}$ limit but use the parameterisations to extrapolate over the full kinematic range available (i.e. $M_{\mathrm{cut}} = W_{\gamma p} - M_p$) as was the procedure for measurements made at lower energies, we find a very large variation in the cross section extracted with the various methods (see table 3 for a summary of all the fits). This is because some of the parameterisations assume the ρ^0 resonance to have a long tail extending up to high values of $M_{\pi\pi}$. Unlike the situation at lower energies kinematic constraints do not suppress this tail to levels where it can be neglected.

Model	$M_{cut} = M_\rho + 5\Gamma_0$		$M_{cut} = W_{\gamma p} - M_p$	
	$\sigma_{\pi\pi}$ /μb	σ_ρ /μb	$\sigma_{\pi\pi}$ /μb	σ_ρ /μb
RS +(8)	11.2	9.1	11.2	10.5
RS +(11)	11.4	9.3	11.4	15.9
RS +(12)	11.5	9.2	11.5	13.5
S +(8)	11.2	9.6	10.8	11.4
S +(11)	12.3	8.5	17.0	14.5
S +(12)	11.5	9.6	14.5	14.8

Table 3: The extracted $\sigma(\gamma p \to \pi^+\pi^- p)$ and $\sigma(\gamma p \to \rho^0 p)$ cross sections from the fits of the $\mathrm{d}\sigma/\mathrm{d}M_{\pi\pi}$ spectrum for two choices of $M_{\rm cut}$ (see text) for the low $W_{\gamma p}$ analysis. In the column marked 'Model' RS is the Ross-Stodolsky parameterisation of equation 6, S is the Söding parameterisation of equation 9. The bracketed numbers refer to the equation describing the momentum dependent width.

Since it was not possible to determine the $M_{\pi\pi}$ and t dependence of the cross section at $\langle W_{\gamma p}\rangle = 187$ GeV, we took the values of $n_{\rm RS}$ and b found in the low $W_{\gamma p}$ analysis[3] to reweight the MC distributions used for the acceptance calculation and to determine numerically ξ (the fraction of the cross section outside the measured region) and the ratio of the cross sections $r_{\rm nr} = \sigma(\gamma p \to \rho^0 p)/\sigma(\gamma p \to \pi^+\pi^- p)$. The values obtained were $\xi = 0.05$ and $r_{\rm nr} = 0.82$. The elastic ρ^0 cross section was then determined using

$$\sigma(\gamma p \to \rho^0 p) = \frac{N - N_{\rm bgd}}{\Phi_I \mathcal{L} \varepsilon} \cdot \frac{1}{1-\xi} \cdot r_{\rm nr}, \qquad (14)$$

where N is the measured number of events in the mass range $0.4 < M_{\pi\pi} < 1.26$ GeV, $N_{\rm bgd}$ is the estimated number of background events, $\Phi_I = 0.00903$ the photon flux found using equation 2, $\mathcal{L}$ is the integrated luminosity and ε is the acceptance. The elastic $\gamma p \to \rho^0 p$ cross section for -0.5 GeV$^2 < t < t_{\rm min}$ and $2M_\pi < M_{\pi\pi} < M_\rho + 5\Gamma_0$ at $\langle W_{\gamma p}\rangle = 187$ GeV is then

$$\sigma(\gamma p \to \rho^0 p) \quad = \quad 13.6 \pm 0.8\,(\text{stat.}) \pm 2.4\,(\text{syst.})\;\mu\text{b}.$$

The breakdown of the various contributions to the systematic error of the elastic ρ^0 cross section measurement at $\langle W_{\gamma p}\rangle = 55$ GeV for the mass range $2M_\pi < M_{\pi\pi} < M_\rho + 5\Gamma_0$ can be found in table 4. The primary source of systematic error comes from the uncertainty of the trigger efficiency, where the large error of 20 % is due to the low statistics in

[3]This procedure is likely to be valid since the measured value of $n_{\rm RS}$ is close to values obtained at lower energies [27, 28, 30], indicating there is little dependence of $n_{\rm RS}$ on $W_{\gamma p}$.

the overlap sample of events used to determine it. An error of 5 % is assigned to the uncertainty in the scanning yield, which was estimated by taking the spread in the yield as found by several scanners. The track fitting error of 4 % was estimated by taking the difference between the acceptances found in data and MC. An error of 3 %, arising mainly from limited statistics, was assigned to the MC acceptance. Changing the t dependence within the errors of the measurement gave a 12 % error. To estimate the error due to background contributions each background was varied by ± 50 % and the $M_{\pi\pi}$ distribution re-fitted. An error of 6 % was assigned to reflect the spread in the extracted cross section due to different assumptions for the parameterisation of the $M_{\pi\pi}$ dependence. The error in the integrated luminosity measurement was 5 %.

Source	Error
Trigger efficiency	20 %
Scanning yield	5 %
Track fit efficiency	4 %
MC acceptance	3 %
GD background	8 %
PD background	5 %
DD background	2 %
ND background	1 %
EL background	1 %
t dependence	12 %
Resonance extraction	6 %
Luminosity	5 %
Total systematic error	28 %

Table 4: Sources of systematic errors for the elastic ρ^0 cross section measurement at $\langle W_{\gamma p}\rangle =$ 55 GeV.

For the high $W_{\gamma p}$ analysis the biggest uncertainty on the elastic ρ^0 cross section measurement comes from background in the elastic ρ^0 sample. A systematic error was taken of 50 % of each background estimated using the MC simulations and 25 % for the electron beam gas background. The error on the electron tagger efficiency was 5 % [3]. An error of 6 % was assigned for the MC acceptance being due to the difference between PHOJET and PYTHIA and the MC statistics. An error of 1 % was found by varying the t slope parameter by ± 4 GeV^{-2} around the central value of 11 GeV^{-2}. The 20 % overall hadronic energy scale uncertainty of the BEMC [31] gave rise to a 4 % error. A 6 % error was assigned to account for the uncertainty in the method of extraction of the resonant cross section. This error was estimated by taking the spread in the value of the cross section obtained using the results of each fit to the low $W_{\gamma p}$ data as described above, reweighting the input MC $M_{\pi\pi}$ distributions and recalculating the acceptances and values for ξ and $r_{\rm nr}$. The error in the integrated luminosity measurement was 5 %. A breakdown of the systematic error is shown in table 5.

Source	Error
GD background	9 %
PD background	4 %
DD background	2 %
ND background	1 %
EL background	7 %
MC acceptance	6 %
BEMC hadronic scale	4 %
t dependence	1 %
e-gas background	5 %
e-tagger acceptance	5 %
Resonance extraction	6 %
Luminosity	5 %
Total systematic error	18 %

Table 5: Sources of systematic errors for the elastic ρ^0 cross section measurement at $\langle W_{\gamma p}\rangle =$ 187 GeV.

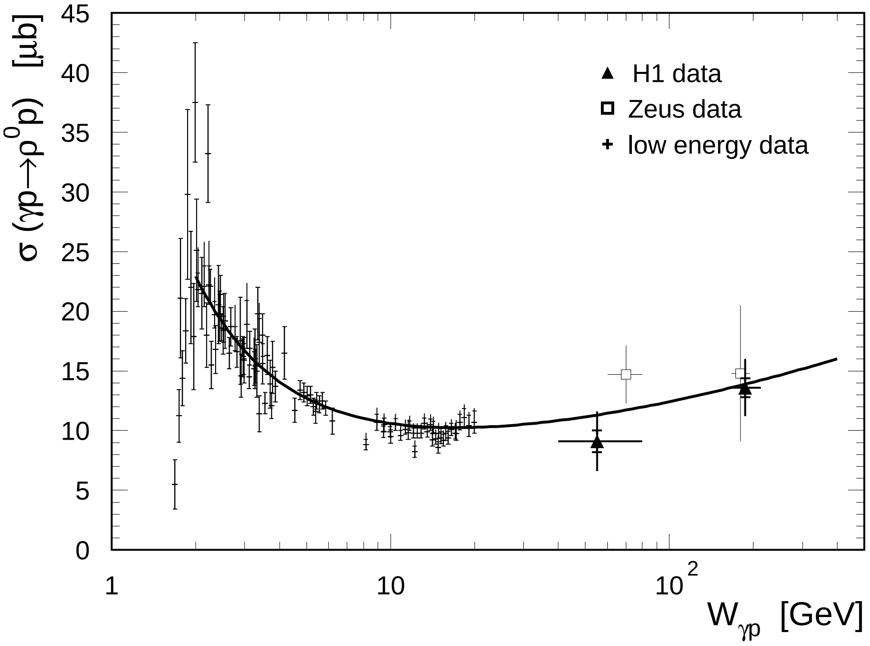

Figure 6: The dependence of the elastic ρ^0 photoproduction cross section, $\sigma(\gamma p \to \rho^0 p)$, on $W_{\gamma p}$ for H1 and previous measurements [2, 6, 32, 33]. The inner vertical bars on the H1 points denote only the statistical error, the outer ones contain statistical and systematic errors added in quadrature. The horizontal error bars show the range in $W_{\gamma p}$ over which the measurements were made. The solid curve shown is a curve based on a soft pomeron calculation, the normalisation of which is fixed by the data at low energy [11].

Figure 6 summarises the dependence on $W_{\gamma p}$ of measurements of the elastic ρ^0 photoproduction cross section [2, 6, 32, 33] including our new measurements. Also shown is the theoretical prediction based on the VMD model and non-perturbative Regge theory [11] (solid curve). The new high energy measurements at HERA demonstrate that the $W_{\gamma p}$ dependence of the cross section is consistent with the slight increase characteristic of this model in which the leading exchange is a 'soft' pomeron.

6.3 The t Dependence of the Elastic ρ^0 Photoproduction Cross Section

Diffractive scattering is characterised by a low momentum transfer between the vector meson and the proton, resulting in a steeply falling distribution in t. This is quantified by the slope parameter, b, determined by fitting the form e^{bt} to the t dependence of $d\sigma/dt$ for the data taken at $\langle W_{\gamma p}\rangle = 55$ GeV.

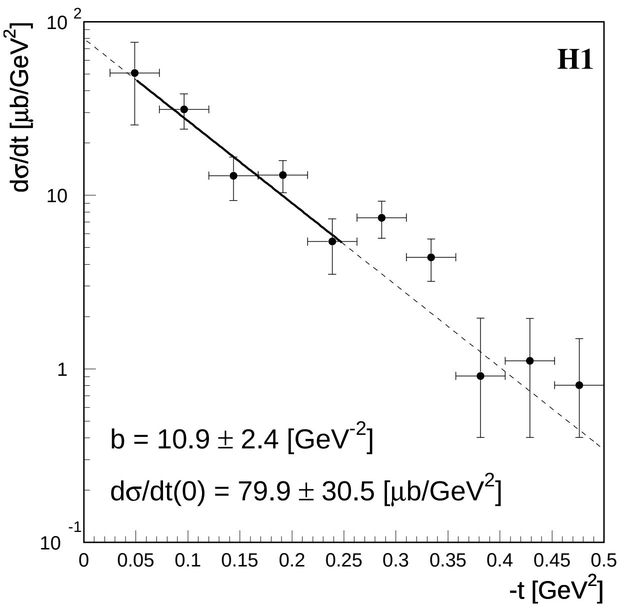

Figure 7: The differential cross section, $d\sigma/dt$, at $\langle W_{\gamma p}\rangle = 55$ GeV is fitted over the range $0.025 < |t| < 0.25$ GeV^2 with the function $d\sigma/dt = a\, e^{bt}$ (only statistical errors are shown).

The cross section $d\sigma/dt$ was determined by integrating the mass spectrum over the measured range ($0.52 < M_{\pi\pi} < 1.17$ GeV) and correcting for losses and backgrounds using the MC simulation. A correction was made for losses in the tails making the assumption that $n_{\rm RS}$, the Ross-Stodolsky parameter, remained constant with t, so that $\xi = 0.15$ at each value of t. The results are shown in figure 7. The data for $0.025 < |t| < 0.25$ GeV^2 are well parameterised with a simple exponential with slope parameter

$$b = 10.9 \pm 2.4\,(\text{stat.}) \pm 1.1\,(\text{syst.})\ \text{GeV}^{-2}$$

and intercept

$$\left.\frac{\mathrm{d}\sigma(\gamma p \to \rho^0 p)}{\mathrm{d}t}\right|_{t=0} = 79.9 \pm 30.5\,(\mathrm{stat.}) \pm 21.9\,(\mathrm{syst.})\ \mu\mathrm{b/GeV}^2.$$

The systematic error arises from the variation of the MC input parameters for the skewing of the line shape and the b slope within the statistical errors of the fits and also by allowing each background to vary by 50 %. For the intercept the systematic errors on the normalisation are also taken into account (see section 6.2). For $|t| > 0.25$ GeV^2, deviations from a simple exponential dependence were shown by other measurements of diffractive vector meson photoproduction [27, 28, 34].

The measurement of b is compared to previous determinations in figure 8. The recent ZEUS measurement [6] is shown along with lower energy data as compiled by Aston et al. [27, 28, 29, 30, 35]. The ZEUS and H1 results together show that the shrinkage of the t dependence of $\mathrm{d}\sigma/\mathrm{d}t$ continues into the HERA energy range as expected in the soft pomeron picture.

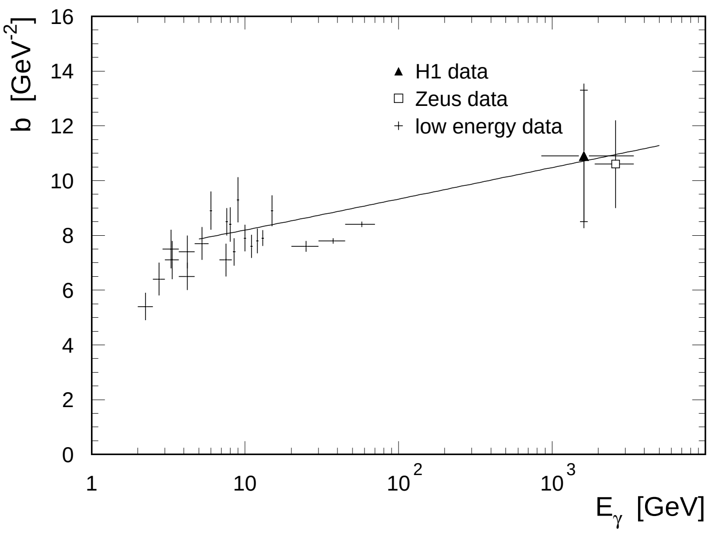

Figure 8: Determinations of the exponential slope parameter, b, as a function of E_γ, the photon energy in the rest frame of the proton. The inner vertical bar on the H1 point denotes the statistical error only, the outer one contains statistical and systematic errors added in quadrature. The horizontal error bars show the range in $W_{\gamma p}$ over which the measurements were made. The curve is a prediction based on pomeron exchange [11].

6.4 Polar Angular Decay Distribution of the ρ^0

A feature of the diffractive production of hadrons, in addition to a slight dependence of the cross section on $W_{\gamma p}$ and a peripheral t dependence, is s-channel helicity conservation. This is best studied in the helicity frame, defined as the rho meson rest frame, with the quantisation axis along the direction of the rho in the γp frame [22]. In this frame, the

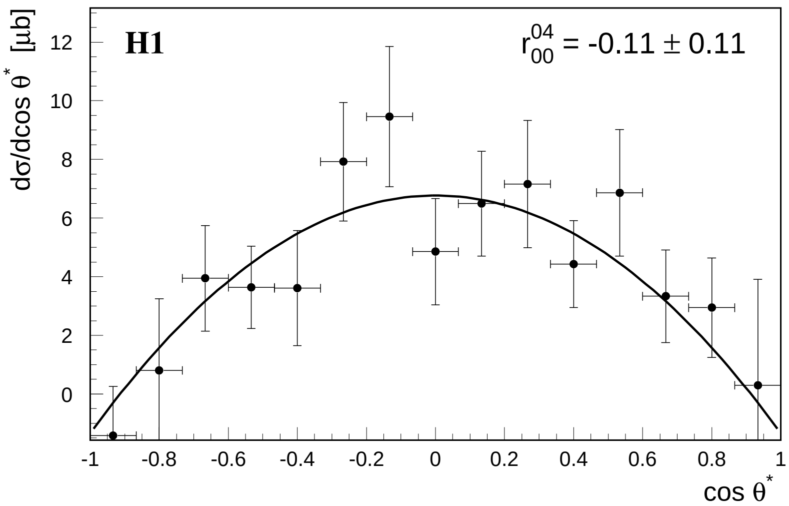

Figure 9: The acceptance corrected $\cos\theta^*$ density distribution at $\langle W_{\gamma p}\rangle = 55$ GeV. The data are fitted to the function in equation 16. The errors quoted are only statistical.

polar angle distribution of the π^+ according to the formalism in [36, 9] is

$$\frac{\mathrm{d}\sigma}{\mathrm{d}\cos\theta^*} \propto (3r^{04}_{00} - 1)\cos^2\theta^* + (1 - r^{04}_{00}), \tag{15}$$

where r^{04}_{00} is the spin density matrix element which specifies the probability that the ρ^0 meson is produced in the spin substate 0.

In order to determine r^{04}_{00}, the distribution in $\cos\theta^*$ was obtained using the same selection, subtraction and correction procedures as for the $\mathrm{d}\sigma/\mathrm{d}t$ analysis. The expression 15 was then fitted to this distribution to obtain a value of

$$r^{04}_{00} = -0.11 \pm 0.11\,(\mathrm{stat.}) \pm 0.04\,(\mathrm{syst.}).$$

Figure 9 shows $\mathrm{d}\sigma/\mathrm{d}\cos\theta^*$ and the fit of the expression 15. In the helicity frame the ρ^0 is thus observed to be produced predominantly in spin substates ± 1 and not in spin substate 0, consistent with the hypothesis of s-channel helicity conservation at $Q^2 = 0$.

7 Conclusions

With the H1 detector we have measured the cross section for the elastic photoproduction of ρ^0 mesons and found $\sigma(\gamma p \to \rho^0 p) = 9.1 \pm 0.9\,(\mathrm{stat.}) \pm 2.5\,(\mathrm{syst.})$ μb at $\langle W_{\gamma p}\rangle =$ 55 GeV and $\sigma(\gamma p \to \rho^0 p) = 13.6 \pm 0.8\,(\mathrm{stat.}) \pm 2.4\,(\mathrm{syst.})$ μb at $\langle W_{\gamma p}\rangle = 187$ GeV for $2M_\pi < M_{\pi\pi} < M_\rho + 5\Gamma_0$. At the former $W_{\gamma p}$, the slope parameter of the distribution in t is $10.9 \pm 2.4\,(\mathrm{stat.}) \pm 1.1\,(\mathrm{syst.})$ GeV^{-2} and the decay polar angular distribution is consistent with a pure $\sin^2\theta^*$ distribution. We thus verify the extension to HERA energies of the properties found at lower energies for elastic photoproduction of the ρ^0 meson, namely a steep forward distribution of the produced ρ^0 mesons with a continued shrinkage of the t dependence with increasing $W_{\gamma p}$ and a decay angular distribution that is consistent with s-channel helicity conservation. A slow rise of the elastic ρ^0 cross section with $W_{\gamma p}$, as expected in a picture of interactions based upon the soft pomeron which also matches the rise of the total photoproduction cross section, is shown to be consistent with observation.

Acknowledgements

We are grateful to the HERA machine group whose outstanding efforts made this experiment possible. We appreciate the immense effort of the engineers and technicians who constructed and maintained the detector. We thank the funding agencies for their financial support of the experiment. We wish to thank the DESY directorate for the support and hospitality extended to the non-DESY members of the collaboration.

References

[1] H1 Collaboration, T. Ahmed et al., Phys. Lett. B299 (1993) 374.

[2] ZEUS Collaboration, M. Derrick et al., Z. Phys. C63 (1994) 391.

[3] H1 Collaboration, S. Aid et al., Z. Phys. C69 (1995) 27

[4] H1 Collaboration, T. Ahmed et al., Phys. Lett. B338 (1994) 507.

[5] ZEUS Collaboration, M. Derrick et al., Phys. Lett. B350 (1995) 120.

[6] ZEUS Collaboration, M. Derrick et al., "Measurement of Elastic ρ^0 Photoproduction at HERA" DESY preprint 95-143 (1995).

[7] ZEUS Collaboration, M. Derrick et al., "Measurement of Elastic ϕ Photoproduction at HERA" DESY preprint 96-002 (1996).

[8] J. J. Sakurai, Phys. Rev. Lett. 22 (1969) 981;
J. J. Sakurai and D. Schildknecht, Phys. Lett. 40B (1972) 121.

[9] T. Bauer, F. Pipkin, R. Spital and D. Yennie, Rev. Mod. Phys. 50 (1978) 261.

[10] P. D. B. Collins, "An Introduction to Regge Theory and High Energy Physics", Cambridge U. P., Cambridge (1977).

[11] G. A. Schuler and T. Sjöstrand, Nucl. Phys. B407 (1993) 539.

[12] B. D. Burow, "A Measurement of the Total Photon-Proton Cross Section in the Center of Mass Energy Range 167 to 194 GeV", Ph. D. Thesis, Dept. of Physics, University of Toronto (1994).

[13] E. J. Williams, Proc. Roy. Soc. London A139 (1933) 163;
C. F. Weizsäcker, Z. Phys. 88 (1934) 612.

[14] H1 Collaboration, I. Abt et al., “The H1 Detector at HERA”, DESY preprint 93-103 (1993).

[15] T. Sjöstrand, Comp. Phys. Comm. 39 (1986) 347;
T. Sjöstrand and M. Bengtsson, Comp. Phys. Comm. 43 (1987) 367;
T. Sjöstrand and M. Bengtsson, Comp. Phys. Comm. 46 (1987) 43.

[16] R. Engel, Proceedings of the XXIXth Rencontre de Moriond (1994) 321.

[17] R. Engel, Z. Phys. C66 (1995) 203.

[18] T. Wolff et al., Nucl. Instr. and Meth. A323 (1992) 537.

[19] S. Eichenberger et al., Nucl. Instr. and Meth. A323 (1992) 532.

[20] T. J. Chapin et al., Phys. Rev. D31 (1984) 17.

[21] M. Ross and L. Stodolsky, Phys. Rev. 149 (1966) 1172.

[22] J. D. Jackson, Il Nuovo Cimento 34 (1964) 1644.

[23] Particle Data Group, Phys. Rev. D50 (1994) 1173.

[24] R. Spital and D. R. Yennie, Phys. Rev. D9 (1974) 126.

[25] P. Söding, Phys. Lett. 19 (1966) 702.

[26] S. Drell, Phys. Rev. Lett. 5 (1967) 278.

[27] D. Aston et al., Nucl. Phys. B209 (1982) 56.

[28] G. Gladding et al., Phys. Rev. D8 (1973) 3721.

[29] G. McClellon et al., Phys. Rev. Lett. 22 (1969) 374.

[30] Y. Eisenberg et al., Phys. Rev. D5 (1972) 15.

[31] H1 Collaboration, T. Ahmed et al., Nucl. Phys. B439 (1995) 471.

[32] A. Baldini et al., “Numerical Data and Functional Relationships in Science and Technology. Grp. 1: Nuclear and Particle Physics. Vol. 12: Total Cross-sections for Reactions of High-energy Particles (Including Elastic, Topological, Inclusive and Exclusive Reactions)”, Landolt-Börnstein’s New Series, 1/12B, Berlin (1988) 345.

[33] P. Callahan et al., “Rho Photoproduction from 45-GeV TO 225-GeV”, preprint FERMILAB-PUB-84/36-E (1984).

[34] D. P. Barber et al., Z. Phys. C12 (1982).

[35] C. Berger et al., Phys. Lett. B39 (1972) 659.

[36] K. Schilling and G. Wolf, Nucl. Phys. B61 (1973) 381.